Characterization of prompt gamma-ray emission with respect to the Bragg peak for proton beam range verification: A Monte Carlo study

Melek Zarifi[a], Susanna Guatelli[a], David Bolst[a], Brian Hutton[b], Anatoly Rosenfeld[a], Yujin Qi[a*]

[a] Centre for Medical Radiation Physics, University of Wollongong, NSW, Australia

[b] Institute of Nuclear Medicine, University College London, London, UK

*Corresponding Author: Yujin Qi, email: yujin@uow.edu.au

Abstract

In this paper we report a Geant4 simulation study to investigate the characteristic prompt gamma (PG) emission in a water phantom for real-time monitoring of the Bragg peak (BP) during proton beam irradiation. The PG production, emission spatial correlation with the BP, and position preference for detection with respect to the BP have been quantified in different PG energy windows as a function of proton pencil-beam energy from 100 to 200 MeV. The PG response to small BP shifts was evaluated using a 2 cm-thick slab with different human body materials embedded in a water phantom. Our results show that the prominent characteristic PG emissions of 4.44, 5.21 and 6.13 MeV exhibit distinctive correlation with the dose deposition curve. The accuracy in BP position identification using these characteristic PG rays is highly consistent as the beam energy increases from 100 to 200 MeV. There exists a position preference for PG detection with respect to the BP position, which has a strong dependence on the proton beam energy and PG energies. It was also observed that a submillimeter shift of the BP position can be realized by using PG signals. These results indicate that the characteristic PG signal is sensitive and reliable for BP tracking. Although the maximum of the PG measurement associated with the BP is difficult, it can be optimized with energy and detection position preferences.

Keywords: Prompt Gamma, Bragg Peak, Proton Therapy, Geant4

1. Introduction

The main advantage of proton therapy (PT), as compared to photon radiation therapy, is the finite beam range and localized energy deposition at the Bragg peak (BP) [1]. This provides a unique benefit for cancer radiotherapy, due to highly localized dose deposition to the tumor volume, while sparing critical organs-at-risk and minimizing dose to the normal tissue. However, the advantage of PT has not yet been fully exploited since there exists significant uncertainty [2] in predicting and determining the end-of-range of the beam in the patient during treatment planning and treatment delivery. The beam-range uncertainty could cause the BP to overshoot or undershoot the tumor and damage adjacent healthy tissue. Significant research efforts have been

made in the development of clinically suitable and reliable *in vivo* beam-range verification techniques to ensure PT treatment quality [3].

Current research and development of *in vivo* beam-range verification techniques have mainly focused on the use of secondary prompt and delayed gamma rays that are produced by inelastic proton-nuclear interactions inside the patient [4]. Positron emission tomography (PET) has been adopted in clinical research of PT for post-treatment quality control [5]. It relies on the detection of 511 keV coincident photon pairs from the decay of positron emitting nuclei produced as a result of proton-nuclear interactions [6,7]. The delayed decay via positron emission of the short-lived radioisotopes on the order of 1-15 minutes has several major limitations, such as the inability to offer real-time monitoring, a relatively low yield, the positron range effect and biological washout effect, which affect the quantitative accuracy for beam-range verification. Prompt gamma (PG) rays are emitted almost instantaneously from the decay of the excited nuclear reaction products, which has the major advantage of enabling real-time tracking of the BP during beam delivery with no washout effect [8].

Spectroscopy studies [9] have revealed that proton-induced PG emission exhibits a broad energy spectrum in a wide range of 2-15 MeV and is dominated by a number of characteristic gamma-lines from specific elements of irradiated tissues. These PG rays provide rich information which is not only benefiting for *in vivo* beam-range tracking but also could be utilized to determine the concentration of specific elements such as oxygen within irradiated tumors and healthy tissue over the course of PT treatments [10].

Significant research and development has been made to determine the feasibility of PG imaging for proton beam-range verification. A number of PG measurements of proton pencil beams have been reported, using a single detector [9,11,12], as well as a slit gamma camera [13,14,15] to detect PG signals integrated over a wide energy window between 3 and 6 MeV. Other detectors, such as multi-slit detectors [16] and Compton gamma cameras [17,18] have been proposed, and prototype systems are under development by several groups. Time-of-flight measurements have been identified as an effective way to reduce the interference background induced by neutrons [19].

Although initial studies [11,12] have found a good correlation between the BP position and the PG emission, their correlation relationship has complicated characteristics because they result from different physical processes. There is no exact one-to-one relationship existing between the PG emission and the dose deposition. The energy and intensity of the PG emission are sensitive to the elemental composition of tissues [9,10]. As pointed out in [20] there are many factors influencing the accuracy of beam range estimation using PG emission. Quantitative characterization of the correlation between these factors, particularly with respect to the BP, is of great importance to assess its limitation and aids in the design of a clinically reliable PG imaging system. A recent study from Verburg et al. [21] shows that identifying discrete PG lines could provide several benefits to improve the

accuracy and efficiency of beam-range verification. Quantitative measurements of the characteristic PG rays can be used for precise proton range verification in the presence of tissue with an unknown composition [22].

In this work we focus on several characteristic PG emission lines generated from proton beam irradiation of a water phantom and quantitatively characterize their production and spatial emission correlation with the BP position as a function of proton beam energy. We further evaluate the feasibility of using PG emission lines to track the BP position shifts in a heterogeneous phantom containing slabs of difference body composition materials. This study will provide valuable information for the design and development of a clinically reliable PG imaging system to optimize the PG measurement for real-time BP tracking.

2. Methods

The Geant4 Monte Carlo Toolkit [23,24] (version 10.00) was used to investigate the correlation between the proton beam range and the production of PG rays from proton pencil beams incident on a homogeneous water phantom (density of 1 g/cm^3). The global simulation set-up is shown in Figure 1. A mono-energetic proton pencil beam was used to irradiate the cylindrical water phantom with diameter 30 cm and height 50 cm along its central axis (along the z-axis). The energy deposition was calculated in the phantom along the direction of incidence of the protons so to obtain proton depth-dose curves. Proton beam energies of 100, 120, 140, 160, 180 and 200 MeV were simulated. This energy range was selected as it is typical of a PT treatment. The results can then be extrapolated for Spread-Out Bragg Peaks (SOBP) which originates from the superposition of monochromatic proton beams of different energies in scanning PT. An ideal detecting cylinder surface (called *detection cylinder*), with 100 cm diameter and 50 cm height, coaxially surrounding the phantom, was used to score the secondary gamma rays. The detection cylinder was modelled with its longitudinal axis in coincidence with that of the phantom.

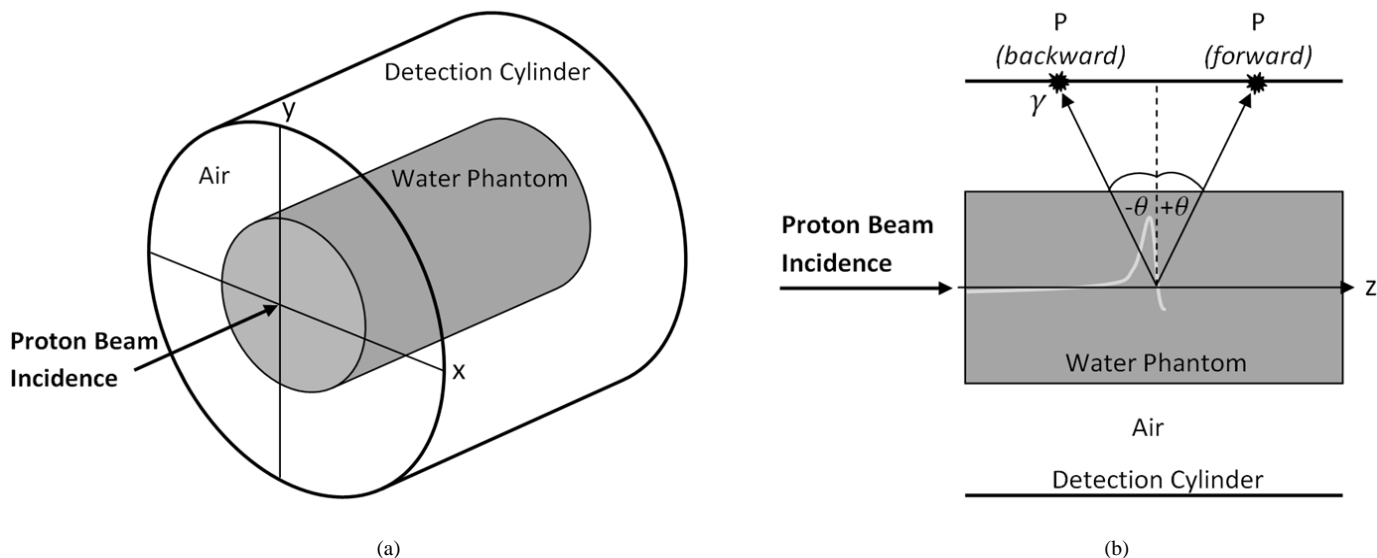(a)   (b)

Figure 1. (a) The geometrical simulation setup of the cylindrical water phantom, in an air-filled detection cylinder coaxially surrounding the phantom. (b) Lateral view of the simulation setup. The angle θ is formed between P, the most probable point on the detector cylinder traversed by the photons, and the normal to the main axis of the phantom passing by the proton beam range R, defined as the point of 50% BP fall-off.

The Geant4 physics list used in this simulation included both electromagnetic (Livermore Low Energy Package) and hadronic physics (QGSP_BIC_HP for protons, neutrons and pions, Binary Ion Cascade model for ions). The Radioactive decay module of Geant4 was active. The QGSP_BIC_HP was chosen as it includes the Binary cascade model which was found adequate for PT studies in [25].

The High Precision Neutron Data Libraries were used to model neutron interactions up to 20 MeV. The output of the simulation consisted of the emission yield Y of the secondary photons along the depth in the phantom. In particular, Y was calculated retrieving the energy and position of the photons when they originate in the phantom. Y was normalized to the number of incident protons on the phantom.

In the post-simulation data analysis, the proton beam range R was defined as the point with 50% BP distal fall-off along the beam path in the phantom. The range extracted from the PG emission (R_{PG}) was defined as the position with 50% PG yield fall-off in the phantom. The difference R-R_{PG}, denoted as Δ *fall-off*, was used to quantify the correlation between PG ray emission and the BP. The energy spectrum of all photons generated in the water phantom, via any physical interaction process was examined. From this spectrum, the prominent PG emission lines were selected with energy windows to study their yield and spatial correlation with respect to the BP.

The position of the gamma rays along the longitudinal axis when reaching the detection cylinder was retrieved from the simulation as well. The distribution of the positions was then fitted and the most frequent position P was determined. P was then used to determine the polar angle θ formed between P and the normal to the main axis of the water phantom, passing through the proton beam range R (see Figure 1(b)). θ allows one to calculate an eventual preferential position, defined with respect to the BP position, to locate the detector to maximize the number of detected PG rays. Positive and negative θ angles mean that the preferential detection position is forward (in the beam direction) and backward (opposite the beam direction) of the BP position, respectively. The results of the simulation are symmetric with respect to the azimuthal coordinate φ as expected.

To study the sensitivity of the PG signal with respect to BP shifts, 2 cm-thick cylindrical slabs of different human body composition materials were inserted in the water phantom upstream of the expected BP. A 200 MeV proton pencil beam was used in this study so as to ensure that the beam passed completely through all the slabs. The materials under study were tissue, muscle, bone and lung. These materials were defined in the simulation from the Geant4 NIST database: tissue ("Adipose Tissue ICRP", density of 0.92 g/cm^3), muscle ("Muscle Striated ICRU", density of 1.04 g/cm^3), bone ("Bone Compact ICRU", density of 1.85 g/cm^3), and lung ("Lung ICRP", density changed to 0.26 g/cm^3 to resemble a lung at end-inhalation). Two scenarios were

considered: (1) one slab of each material in the water phantom; and (2) all four materials were stacked back-to-back in the water phantom to study the combined heterogeneity effect. Figure 2 shows the simulation setup of the two scenarios considered for studying the PG emission deriving from heterogeneous phantoms. A total number of 10^7 incident proton events were simulated for each proton energy and simulation set-up under study to provide suitable statistics.
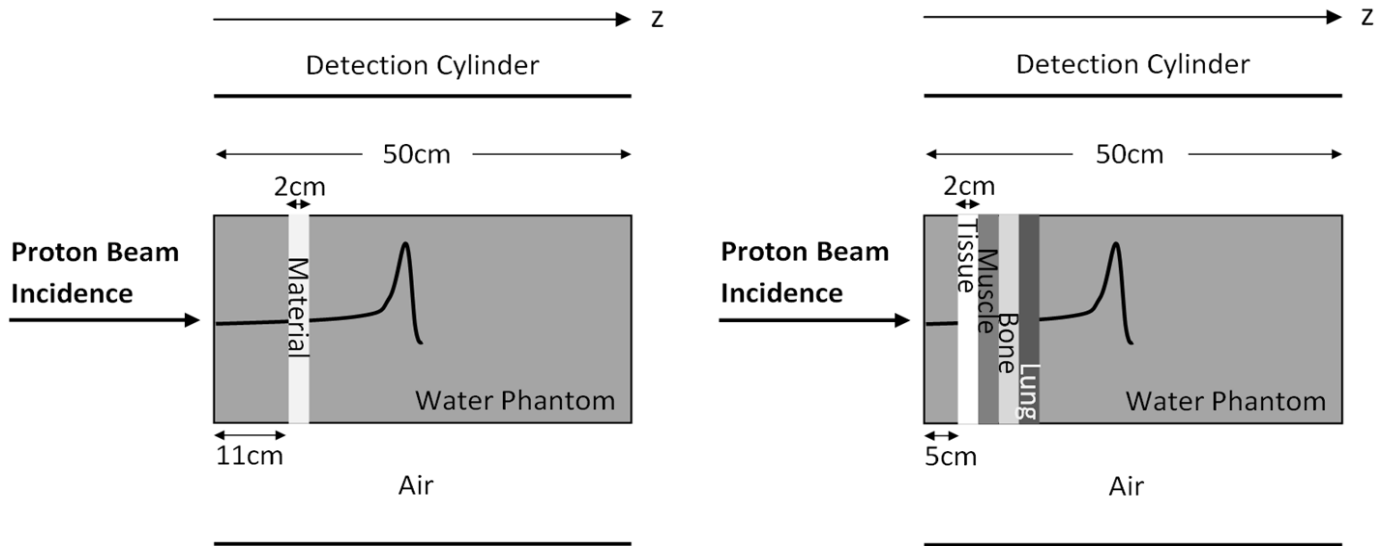

Figure 2. Geometrical simulation setup of the water phantom with 2 cm slabs of tissue, muscle, bone and lung. Two scenarios are considered: a single slab of each material is placed in the water phantom, in the same position for each material (left); and the slabs of materials are placed back-to-back in the water phantom (right).

3. Results

3.1 Energy spectra and yield of prompt gamma emission in the water phantom

Figure 3 shows the energy spectra of photons that originate in the water phantom from any physical interactions (including neutron-induced gamma photons), for three proton beam energies under study. The spectra show consistent shape and characteristics over a wide beam energy range. The energy spectra show several distinguishable emission lines that are produced by non-elastic proton-nuclei interactions with major constituent elements of the phantom material. A peak can be observed in the spectra at 0.511 MeV, originated by the annihilation of positrons resulting from the decay of ^{15}O nuclei. The 2.22 MeV peak results from the capture of secondary thermal neutrons by hydrogen nuclei, and three prominent PG lines are observed with energy 4.44, 5.21 and 6.13 MeV. The 4.44 MeV PG emission line originates from the de-excitation of ^{12}C* nuclei, originating from proton nuclear interactions with oxygen nuclei. The 5.21 and 6.13 MeV PG emission lines derive from ^{15}O* and ^{16}O* de-excitations, respectively. The characteristics of the individual PG lines are investigated by employing three equal-width energy windows of 4.2-4.6 MeV, 5.0-5.4 MeV, and 5.9-6.3 MeV. A larger energy window of 4.2-6.3 MeV is used to study the effect

from all three PG emission lines taken as a whole. An additional wide energy window of 2.0-8.0 MeV, which has been investigated by other groups [17,18], is also used for comparison.
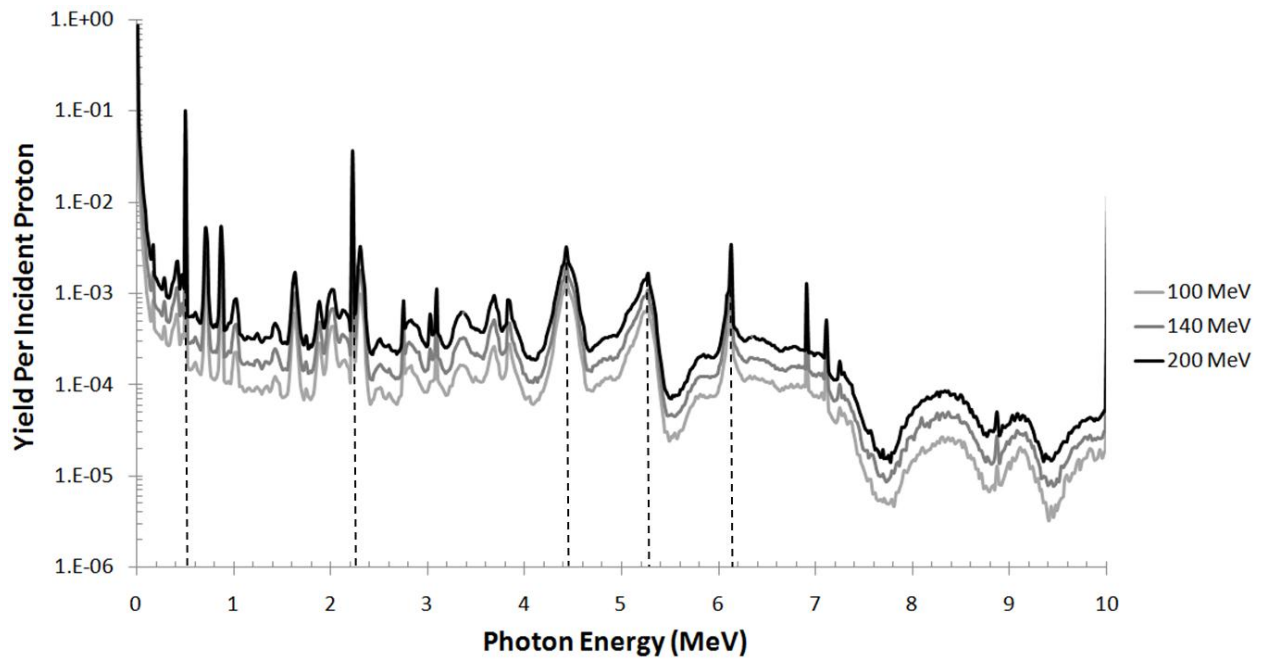

Figure 3. Energy spectra of photons generated in the cylindrical water phantom deriving from proton pencil beams of energy between 100 and 200 MeV. The gamma emission lines are characteristic of those emitted as a result of interactions on the major constituent elements of the phantom material. The PG emission lines of interest are of energy 4.44 MeV, 5.21 MeV and 6.13 MeV, generated by excited ^{12}C, ^{15}O and ^{16}O nuclei, respectively.

The yields in different photon energy windows for PG rays originating from the water phantom per incident proton are estimated and listed in Table 1. As expected, the PG yield increases with higher proton beam energy. For all the proton beam energies considered, the most abundant PG emission yield is found in the energy window between 4.2 and 6.3 MeV. The energy window 4.2-4.6 MeV has a higher yield than 5.0-5.4 MeV and 5.9-6.3 MeV.

Table 1. Gamma photon yields obtained in different PG energy windows. The PG rays originate inside the water phantom. The statistical uncertainty affecting the results is within 1%.

Proton Beam Energy (MeV)	Photon Energy Window (MeV)	Photon Yield Per Incident Proton (%)
100	No window	39.64
	2.0-8.0	5.61
	4.2-4.6	1.14
	5.0-5.4	0.71
	5.9-6.3	0.40
	4.2-6.3	2.59
120	No window	56.75
	2.0-8.0	7.55
	4.2-4.6	1.40
	5.0-5.4	0.90
	5.9-6.3	0.53
	4.2-6.3	3.28
140	No window	75.39
	2.0-8.0	9.70
	4.2-4.6	1.67
	5.0-5.4	1.10
	5.9-6.3	0.66
	4.2-6.3	4.00
160	No window	95.20
	2.0-8.0	11.94
	4.2-4.6	1.95
	5.0-5.4	1.30
	5.9-6.3	0.80
	4.2-6.3	4.74
180	No window	115.99
	2.0-8.0	14.36
	4.2-4.6	2.24
	5.0-5.4	1.51
	5.9-6.3	0.95
	4.2-6.3	5.52
200	No window	137.40
	2.0-8.0	16.85
	4.2-4.6	2.53
	5.0-5.4	1.72
	5.9-6.3	1.09
	4.2-6.3	6.30

3.2 Spatial correlation between prompt gamma emission and the proton beam range

The simulation results showed that the ranges of protons with energy between 100 and 200 MeV in water are from approximately 76 mm to 258 mm. Figure 4 shows the longitudinal yield distribution of PG emission in an energy window of 2.0-8.0 MeV. The Bragg curve is plotted as well to show the correlation between PG and the BP. It can be observed that the total PG emission yield integrated over the 2.0-8.0 MeV energy window is relatively flat in the proton dose plateau and decreases rapidly near the proton end-of-range, regardless of the proton beam energy. The PG fall-off exhibits a close correspondence with the BP fall-off, which has been proposed for real-time BP tracking in PT. This observation agrees well with the experimental results from other research groups [11,12].
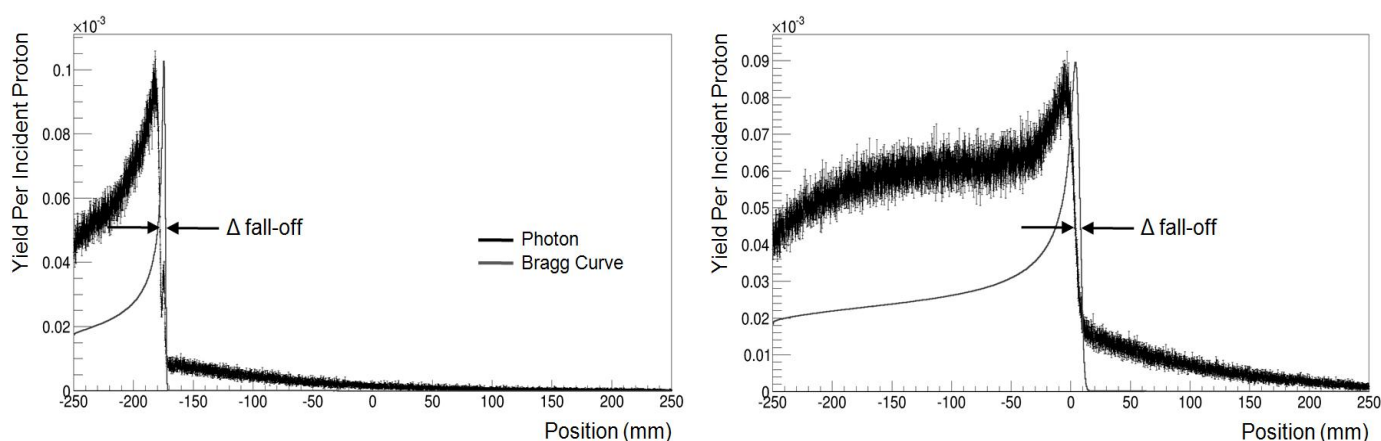

Figure 4. Longitudinal normalized yield distribution of PG rays in the energy window of 2.0-8.0 MeV with the Bragg curve in the water phantom, for 100 MeV (left) and 200 MeV (right) proton pencil-beam energies. The Bragg peak is normalized to the maximum of the gamma yield (the scale on the vertical-axis is arbitrary for the Bragg curve). The arrows indicate the *Δ fall-off* as defined in Section 2.

Figure 5 shows the longitudinal distributions of characteristic PG rays in different energy windows produced in the water phantom with the corresponding Bragg peak, for proton beam energy of 200 MeV. All the three characteristic PG rays show a distinctive correlation with the Bragg curve but different precision for BP tracking. The 4.44 MeV PG rays in the 4.2-4.6 MeV window exhibit an emission distribution very similar to the Bragg curve shape and show sharp peak and fall-off near the end of the proton range. The 5.21 MeV PG rays in the 5.0-5.4 MeV window show a peak at a depth further from the BP. The 6.13 MeV PG rays in the energy window of 5.9-6.3 MeV exhibit the closest emission fall-off correlation with the BP but significantly lower PG yield than the other two PG lines. Yet the combined PG window of 4.2-6.3 MeV, which integrates the three PG emission lines, shows similar accuracy in the PG peak (as compared to the BP) as the 4.2-4.6 MeV window since the 4.44 MeV PG has a dominant yield.
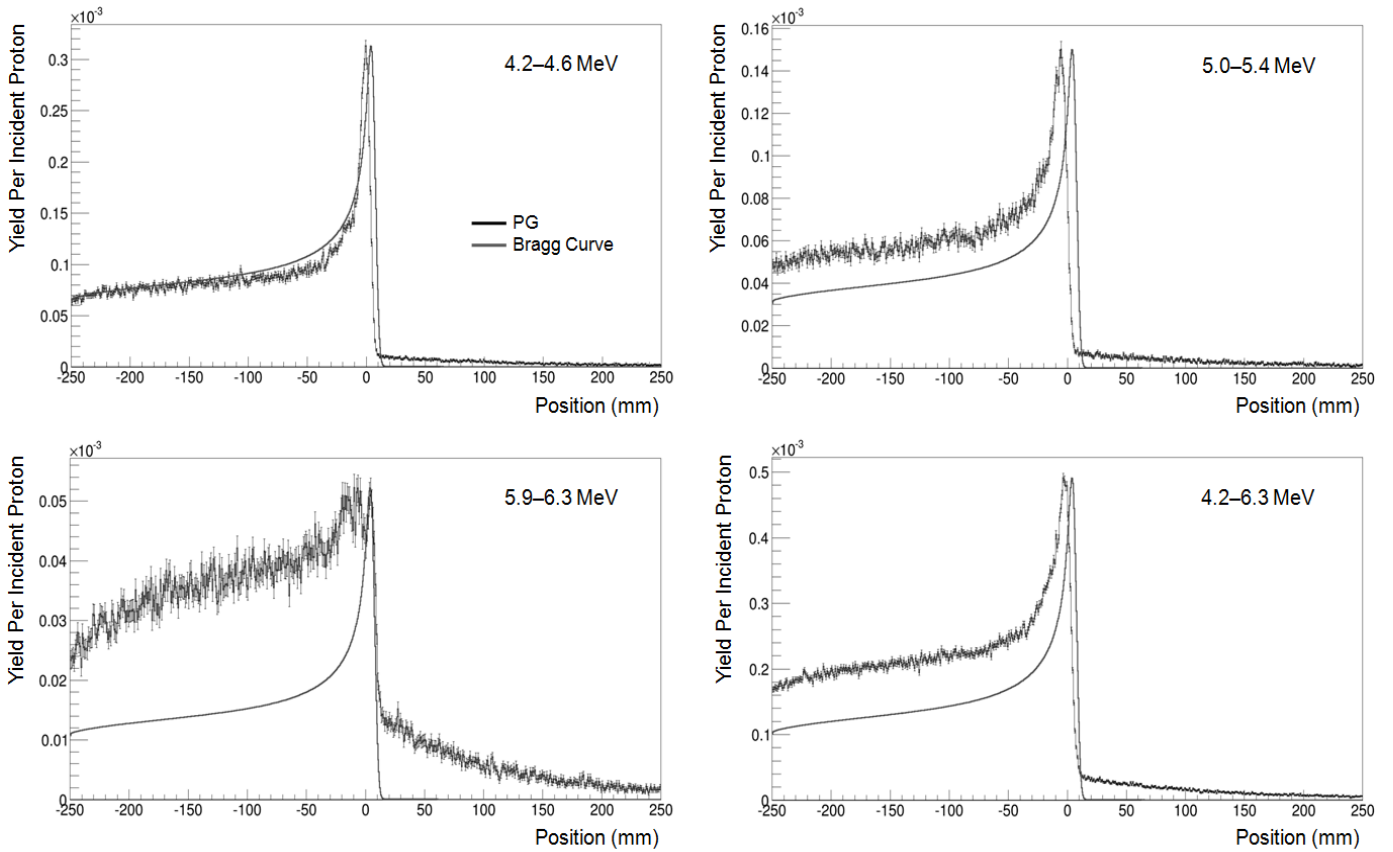
Figure 5. Longitudinal PG yield distribution correlation with the Bragg curve in the water phantom from different gamma energy windows with an incident 200 MeV proton pencil beam. The Bragg peak is normalized to the maximum of the gamma yield (the scale on the vertical-axis is arbitrary for the Bragg curve).

The quantified difference, Δ *fall-off,* between 50% PG fall-off and proton beam range has been extracted from Figure 5. Figure 6 shows the Δ *fall-off* to predict the proton beam range in the water phantom as a function of the energy of the incident proton beam. It can be observed that the three characteristic PG rays of 4.44, 5.21 and 6.13 MeV provide different range verification accuracy. The 6.13 MeV PG rays provide the highest accuracy of around 1 mm, however the yield of these PG rays is the lowest (see Table 1). The 5.21 MeV PG rays provide accuracy of around 8 mm while the 4.44 MeV PG rays provide accuracy of 4-5 mm. The combined 4.2-6.3 MeV PG energy window exhibits similar Δ *fall-off* values as the 4.44 MeV PG rays. This happens because the 4.2-4.6 MeV energy window is the most dominant in the 4.2-6.3 MeV interval as observed in Section 3.1 (see Table 1), with the benefit of a higher yield. The discrepancy between the BP fall-off and the PG fall-off exhibits a strong dependence on the PG energy window. However, different energy windows have large difference of the PG yields. These pose great challenges to the optimum PG detection requirement.
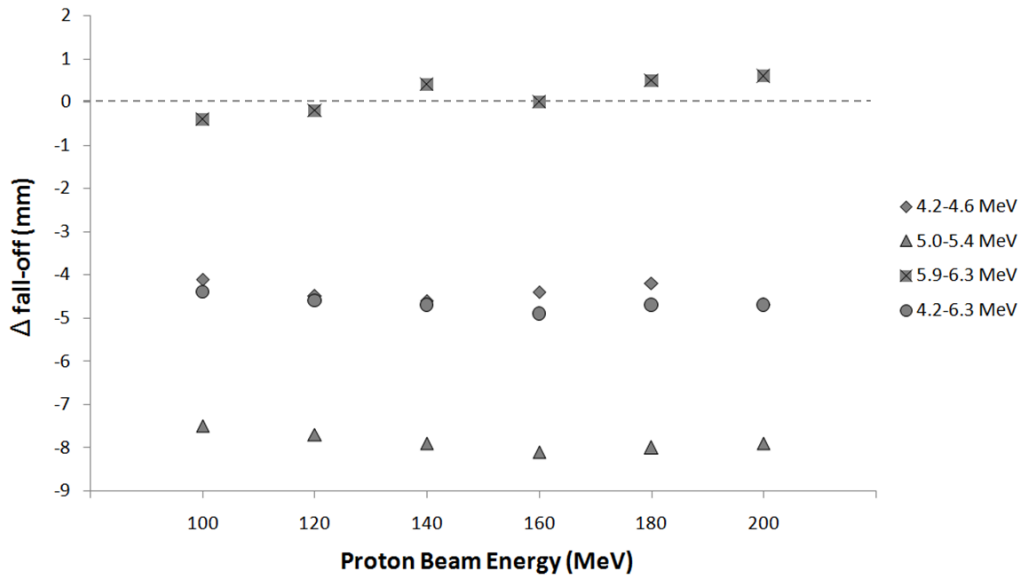
Figure 6. *Δ fall-off*, defined in Section 2, quantifying the accuracy of determination of the proton beam range in the water phantom, as a function of the incident proton beam energy. The positive values represent 50% PG emission fall-off positions occurring after the proton beam range, while negative values before. The statistical uncertainty affecting *Δ fall-off* values is within 0.1 mm.

3.3 Determination of a preferential position for detection of prompt gamma rays with respect to the proton beam range

   With the ideal detection cylinder surrounding the phantom, the number of detectable PG rays can be estimated. The yields of gamma rays that are produced inside the water phantom and reach the detection cylinder for each of the proton beam energies under study are reported in Table 2. As compared to the data in Table 1, it can be observed that the number of gamma photons per incident proton reaching the detection cylinder has significantly decreased, as expected, as they can interact in the water phantom and eventually be absorbed. For each of the beam energies, the 4.2-4.6 MeV energy window has a bigger yield than 5.0-5.4 MeV and 5.9-6.3 MeV. The yield of the entire 4.2-6.3 MeV energy window at the detection cylinder is approximately 25% of the yield of the same gamma rays that originate in the phantom.

Table 2. Detectable gamma photon yields in different energy windows. The PG rays exit the phantom and reach the surface of the detection cylinder. The simulation statistical uncertainty is within 1%.

Proton Beam Energy (MeV)	Photon Energy Window (MeV)	Photon Yield Per Incident Proton (%)
100	No window	4.35
	2.0-8.0	1.47
	4.2-4.6	0.28
	5.0-5.4	0.18
	5.9-6.3	0.10
	4.2-6.3	0.65
120	No window	6.29
	2.0-8.0	2.01
	4.2-4.6	0.35
	5.0-5.4	0.23
	5.9-6.3	0.14
	4.2-6.3	0.85
140	No window	8.55
	2.0-8.0	2.64
	4.2-4.6	0.44
	5.0-5.4	0.29
	5.9-6.3	0.18
	4.2-6.3	1.07
160	No window	10.98
	2.0-8.0	3.28
	4.2-4.6	0.52
	5.0-5.4	0.35
	5.9-6.3	0.23
	4.2-6.3	1.30
180	No window	13.71
	2.0-8.0	4.00
	4.2-4.6	0.60
	5.0-5.4	0.41
	5.9-6.3	0.27
	4.2-6.3	1.53
200	No window	16.52
	2.0-8.0	4.74
	4.2-4.6	0.69
	5.0-5.4	0.48
	5.9-6.3	0.32
	4.2-6.3	1.77

Figure 7 shows a typical longitudinal distribution of PG rays registered on the surface of the detection cylinder. A non-isotropic longitudinal distribution of PG rays is observed, as expected. There is no sharp fall-off at the position of the proton beam range. It shows that there exists a preferential position in the detection cylinder surface to maximize the geometrical efficiency of PG detection. The data were fitted by a 4th-order polynomial function to determine the maximum position of the PG yield distribution as a preferential detection position. With respect the BP position, this preferential detection position has been quantified with a polar angle θ defined in Figure 1 and in Section 2. For an incident 200 MeV proton beam, θ is $(-15 \pm 1)^{\circ}$, $(-12 \pm 1)^{\circ}$ and $(-11 \pm 1)^{\circ}$ for a PG energy window of 4.2-4.6 MeV, 5.0-5.4 MeV and 5.9-6.3 MeV, respectively. This means that the higher yield of detectable PG rays is found in a location backward of the BP fall-off position.
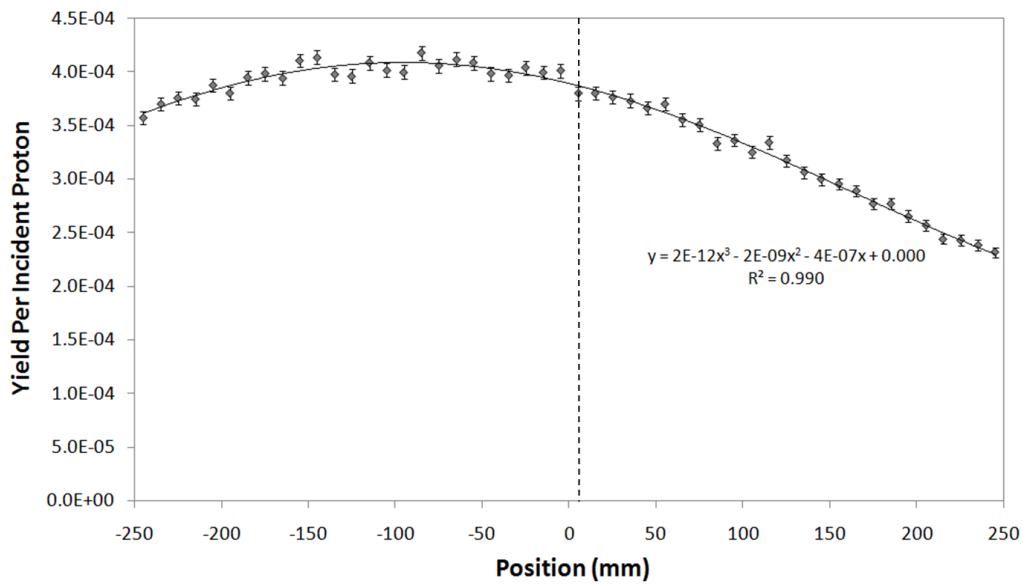

Figure 7. Longitudinal distribution of PG rays in 4.2-6.3 MeV reaching the surface of the detection cylinder once emitted from the water phantom, for an incident 200 MeV proton pencil beam. The data are fitted by a fourth-order polynomial function (solid line). The 50% BP fall-off position in the phantom is indicated with the dash-line.

Figure 8 shows the dependence of the preferential position for PG detection, expressed in terms of θ, on different PG energy windows as a function of the proton beam energy. The preferential position for PG detection shows a strong dependence on the beam energy. As the beam energy increases, the position maximizing the number of detectable PG rays becomes increasingly backward with respect to their BP position. The detection preferential position also shows a considerable variation with PG energy windows. The data show that selecting specific PG energy windows θ changes within 5 degrees only.
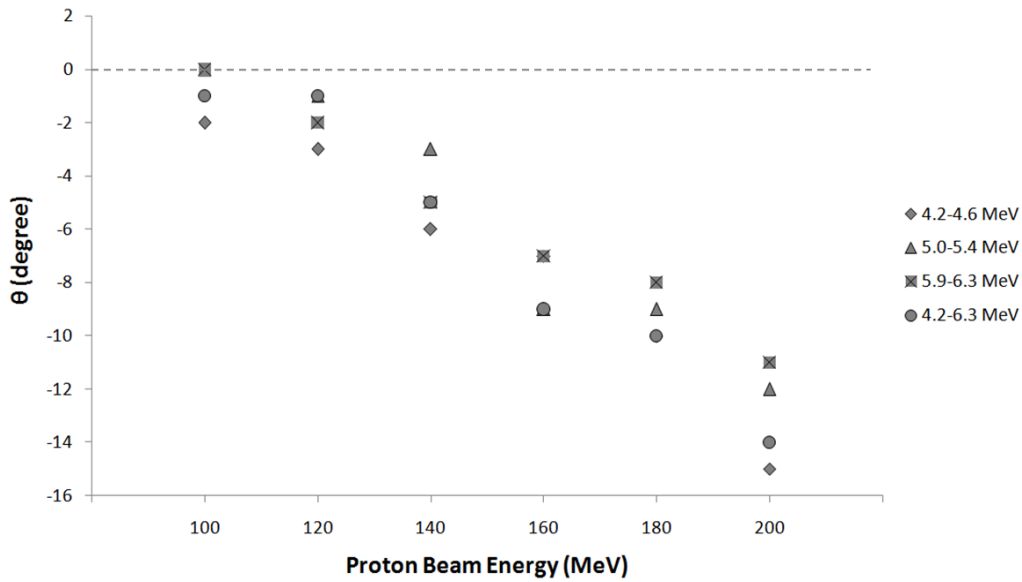
Figure 8. Preferential position for PG detection, quantified in terms of θ (see Figure 1), with respect to the proton beam range. The unceratinly of θ values is estimated around 1°.

3.4 Detection of Bragg peak shift by means of prompt gamma emission: feasibility study

Anatomical heterogeneities were introduced with a slab in the water phantom to evaluate the response of the PG signal to a BP shift. Figures 9 and 10 show the yield of PG rays produced along the depth of the water phantom with single inserts of bone and lung, respectively. These two phantoms are shown because bone and lung exhibit the biggest variation of yields with respect to water. Tissue and muscle show more similar yields to water. The slab's effect on the PG yield is clearly evident at the slab's location (-140 mm to -120 mm) in Figures 9 and 10, which shows a close correspondence to the dose deposition variation at the slab location. Figure 11 shows the yield distribution of PG rays with all four material slabs stacked together (-200 mm to -120 mm).

It can be observed that the PG yield becomes maximum and then falls off close to the BP, as found in the case of the homogeneous water phantom. The yield of PG rays is found to be dependent on the material composition and density of the medium traversed by the proton beam. Bone comprises of ~28% carbon, ~41% oxygen and ~6% hydrogen, whereas lung comprises of ~10% carbon, ~76% oxygen and ~10% hydrogen. Tissue comprises of ~64% carbon, ~23% oxygen and ~12% hydrogen, and muscle comprises of ~12% carbon, ~73% oxygen and ~10% hydrogen. As expected, the PG ray yield increases with density. The PG ray emission yield is lowest for lung and maximum for bone for the set of materials under study.
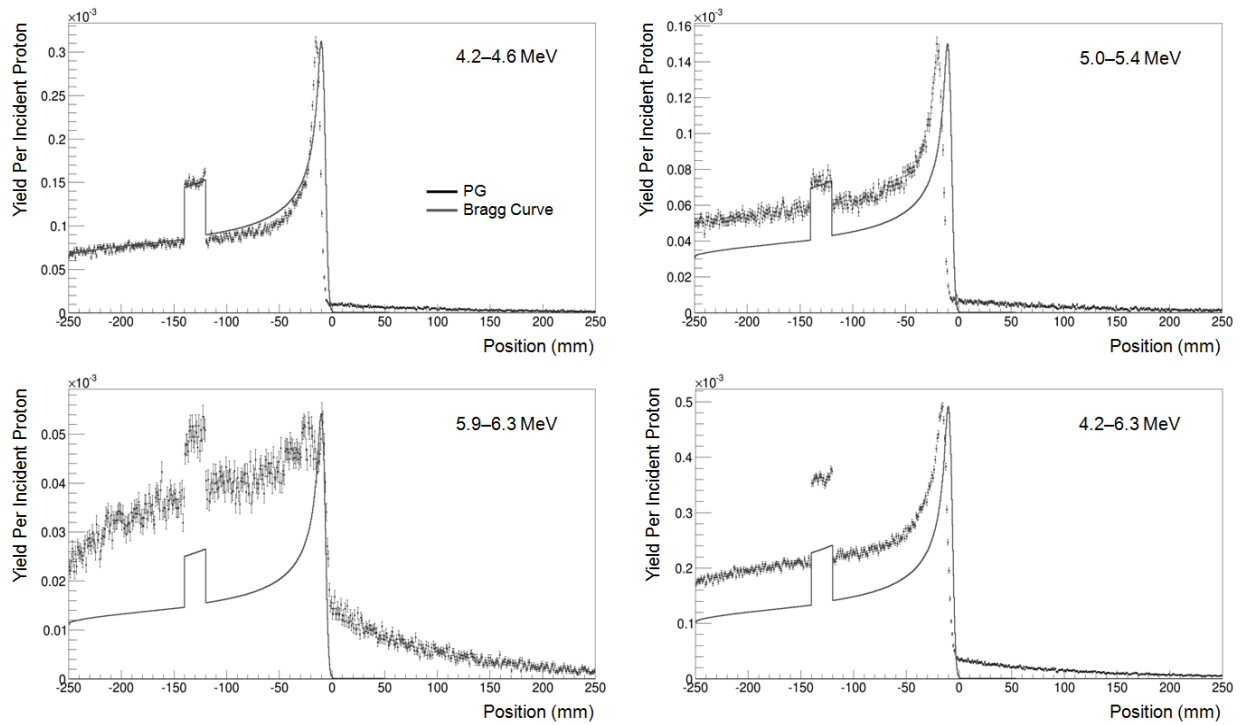
Figure 9. Longitudinal yield distribution of PG rays when they originate in the water phantom with the slab of bone material at the location of -140 mm to -120 mm. The Bragg peak is normalized to the maximum of the PG yield (the scale on the vertical-axis is arbitrary for the Bragg curve). The beam energy is 200 MeV and the PG energy window is indicated in each graph.
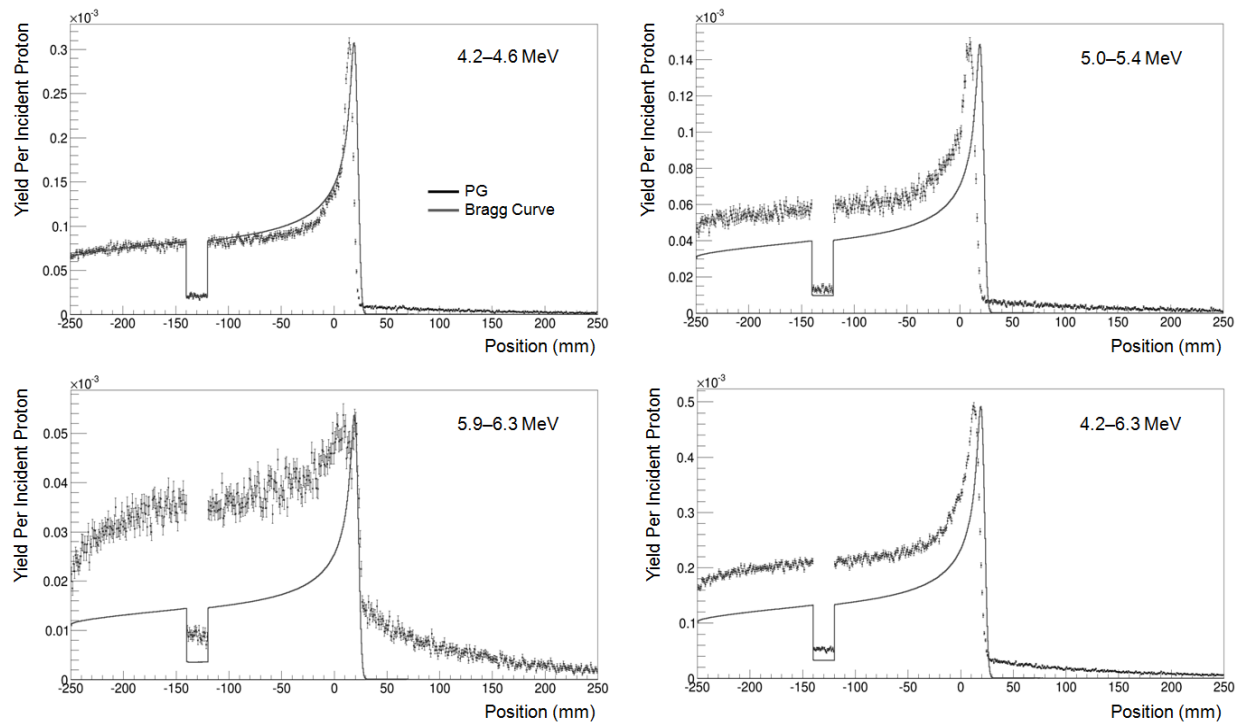

Figure 10. Longitudinal yield distribution of PG rays when they originate in the water phantom with the slab of lung material at the location of -140 mm to -120 mm. The Bragg peak is normalized to the maximum of the PG yield (the scale on the vertical-axis is arbitrary for the Bragg curve). The beam energy is 200 MeV and the PG energy window is indicated in each graph.
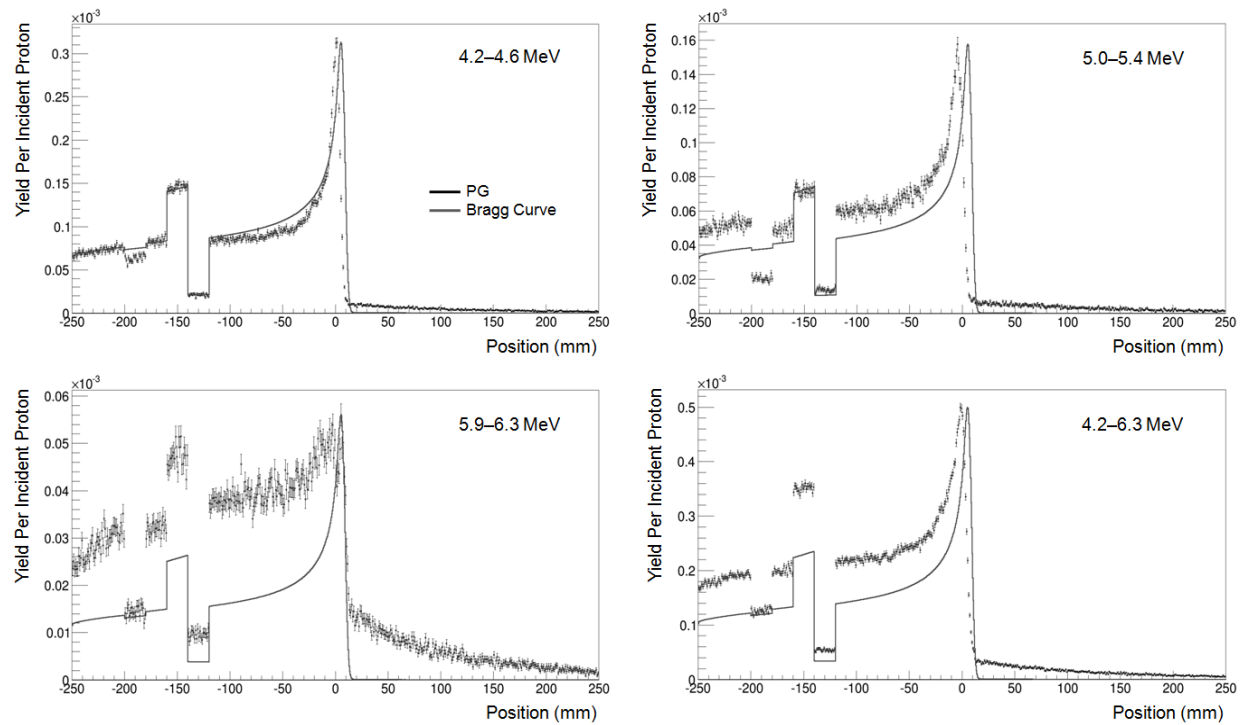
Figure 11. Longitudinal distribution of the yield of PG rays when they originate in the water phantom with all four stacked materials (tissue, muscle, bone and lung) at the location of -200 mm to -120 mm. The Bragg peak is normalized to the maximum of the PG yield (the scale on the vertical-axis is arbitrary for the Bragg curve). The beam energy is 200 MeV and the PG energy window is indicated in each graph.

Table 3 reports the range of a 200 MeV proton beam in the water phantom with the insertion of different material slabs, as calculated by the Geant4 simulation. The suitability to use a PG emission signal to track BP position shifts is quantified by comparing the results of the slab-embedded water phantom with the homogeneous water phantom. It is observed that both bone and lung slabs cause a large shift in the BP position, greater than 10 mm. The PG signal is capable of tracking this shift with high accuracy. Tissue and muscle slabs cause a small shift in the BP position, less than 1 mm. The PG signal is also capable of detecting this submillimeter shift in the proton beam range.

Table 3. Comparison of BP shifts and the PG fall-off shifts between the slab-embedded water phantom and the homogeneous water phantom from the 200 MeV proton pencil-beam irradiation.

Phantom	Proton Beam Range (± 0.1 mm)	Shift in Proton Beam Range (± 0.1 mm)	PG Energy Window (MeV)	50% PG Emission Fall-off (± 0.1 mm)	Shift in 50% PG Emission Fall-off (± 0.1 mm)
Water (homogeneous)	258.2	−	2.0-8.0	254.1	−
			4.2-4.6	253.5	−
			5.0-5.4	250.3	−
			5.9-6.3	258.8	−
			4.2-6.3	253.5	−
Tissue Slab	258.9	0.7	2.0-8.0	254.9	0.8
			4.2-4.6	254.3	0.8
			5.0-5.4	250.6	0.3
			5.9-6.3	259.3	0.5
			4.2-6.3	254.3	0.8
Muscle Slab	257.7	-0.5	2.0-8.0	253.4	-0.7
			4.2-4.6	253.1	-0.4
			5.0-5.4	249.8	-0.5
			5.9-6.3	258.0	-0.8
			4.2-6.3	253.3	-0.2
Bone Slab	244.0	-14.2	2.0-8.0	240.0	-14.1
			4.2-4.6	239.2	-14.3
			5.0-5.4	236.2	-14.1
			5.9-6.3	244.6	-14.2
			4.2-6.3	239.4	-14.1
Lung Slab	273.3	15.1	2.0-8.0	268.9	14.8
			4.2-4.6	268.8	15.3
			5.0-5.4	265.5	15.2
			5.9-6.3	273.7	14.9
			4.2-6.3	268.6	15.1
All Material Slabs	259.5	1.3	2.0-8.0	255.3	0.7
			4.2-4.6	254.7	1.2
			5.0-5.4	251.2	0.9
			5.9-6.3	259.9	1.1
			4.2-6.3	254.6	1.1

Figure 12 shows the *Δ fall-off* between the PG emission and the proton beam range for each heterogeneous phantom considered. The results obtained for the homogeneous water phantom are included as well for comparison. It can be observed that the *Δ fall-off* remains consistent for each slab-embedded heterogeneous phantom with a variation less than 1 mm in each of the PG energy windows. These data show that the PG emission signal shifts with the proton beam range to exhibit a consistent correlation to the BP regardless of the material placed in the beam path.
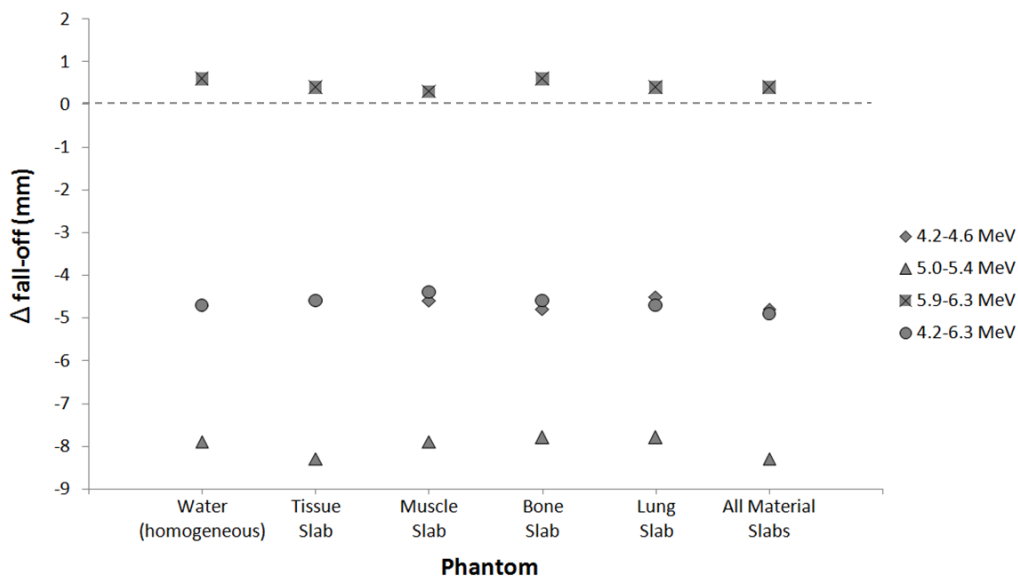

Figure 12. The *Δ fall-off*, defined as the difference between the 50% PG fall-off and the proton beam range, is represented for each phantom under study. The statistical uncertainty affecting the *Δ fall-off* is within 0.1 mm.

4. Discussion and Conclusion

In this work, the emission of three characteristic PG signals (4.44, 5.21 and 6.13 MeV) produced by proton-oxygen nuclear interactions was investigated in a water phantom using Geant4 based simulations. The PG production and detectable yields, spatial correlation of PG longitudinal yield and preferential position for PG detection with respect to the BP as well as using the distal fall-off of the PG longitudinal yield to track BP shifts have been quantified in different PG energy windows as a function of the incident proton beam energy.

The results show that all three characteristic PG emissions exhibit distinctively close correlations with the proton depth-dose curve but offer different precision for beam-range estimations. Either individual or integrated PG emission of the three PG signals can be utilized for BP tracking. The selection of energy window for PG detection has a large effect on the accuracy of proton beam range estimation using PG emission. This is consistent with previous studies [13,20]. The 6.13 MeV PG rays can provide millimeter accuracy but significantly lower PG yield. These results are also in good agreement with the measurements by Verburg et al. [21]. An important finding in this study is that each of the three characteristic PG signals shows a consistent

fall-off difference with respect to the actual beam range in the proton beam energy range of 100-200 MeV. This implies that such PG signals are also well suited for tracking the Spread-Out Bragg Peak.

By virtue of an ideal detection cylinder, the detectable PG yield has been estimated. In the simulation set-up considered, about 25% characteristic PG rays exit the phantom and reach the detection cylinder. The non-isotropic longitudinal distribution of PG emission results in a preferential position for PG detection in the detection cylinder, which could be utilized for maximizing the geometrical efficiency of PG measurement. However, this preferential position has a strong dependence on the beam energy. As the beam energy increases, the position maximizing the number of detectable PG rays gets increasingly backward with respect to their BP position. The detection preferential position also shows a considerable variation with PG energy windows. These make the maximum of the PG detection associated with the BP position difficult. However, the PG measurement can be optimized with energy and detection position preferences. Our results imply that the design of a PG detector with particular energy and geometrical acceptance preferences is desirable. Further work is necessary if the detection of PG associated with the BP is to be optimized with a specific PG detector system.

The PG longitudinal yield variation is sensitive to the elemental composition and the medium density in the heterogenetic phantoms, as also observed in previous work [9,10]. A submillimeter shift of the BP position due to tissue composition variations is clearly evident by the characteristic PG longitudinal yield. This indicates that PG emissions associated with proton interactions in tissue offer the potential for *in vivo* beam-range verification within 1 mm uncertainty, as observed in earlier research [11,14]. But the actual system resolution is mainly determined by the PG detector's property. Our results imply that the detector with PG spectroscopy measurement is favorable for high-precision BP tracking. Further study for the development of a high performance PG detector is under investigation, and the PT PG emission ability to track the position of the BP will be studied with a realistic human phantom in the near future.

Acknowledgement

References

[1] Wilson RR. Radiological use of fast protons. Radiology 1946;47:487-91.
[2] Lomax A J. Intensity modulated proton therapy and its sensitivity to treatment uncertainties 1: the potential effects of calculational uncertainties. Phys. Med. Biol. 2008;53:1027-42.

[3] Richter C, Pausch G, Seco J, Bortfeld T, Enghardt W. Increasing precision in particle therapy: *In vivo* dosimetry and beyond. Phys. Medica. 2014;30:supp.1:e3-e4.

[4] Knopf AC, Lomax A. In vivo proton range verification: a review. Phys. Med. Biol. 2013;58:131-60.

[5] Parodi K, Paganetti H, Shih HA, Michaud S, Loeffler JS, Delaney TF, et al. Patient study of *in vivo* verification of beam delivery and range, using positron emission tomography and computed tomography imaging after proton therapy. Int. J. Radiat. Oncol. Biol. Phys. 2007;68:920-34.

[6] Oelfke U, Lam GK, Atkins MS. Proton dose monitoring with PET: quantitative studies in Lucite. Phys. Med. Biol. 1996;41:177-96.

[7] Parodi K, Enghardt W. Potential application of PET in quality assurance of proton therapy. Phys. Med. Biol. 2000;45:N151-56.

[8] Moteabbed M, Espana S and Paganetti H. Monte Carlo patient study on the comparison of prompt gamma and PET imaging for range verification in proton therapy. Phys. Med. Biol. 2011;56:1063-82.

[9] Polf JC, Peterson S, McCleskey M, Roeder BT, Spiridon A, Beddar S, et al. Measurement and calculation of characteristic prompt gamma ray spectra emitted during proton irradiation. Phys. Med. Biol. 2009;54: N519-27.

[10] Polf JC, Panthi R, Mackin DS, McCleskey M, Saastamoinen A, Roeder BT, Beddar S. Measurement of characteristic prompt gamma rays emitted from oxygen and carbon in tissue-equivalent samples during proton beam irradiation. Phys. Med. Biol. 2013;58:5821-31.

[11] Min CH, Kim CH, Youn MY, Kim JW. Prompt gamma measurements for locating the dose falloff region in the proton therapy. Appl. Phys. Lett. 2006;89:183517.

[12] Testa M, Bajard M, Chevallier M, Dauvergne D, Freud N, Henriquet P, et al. Real-time monitoring of the Bragg-peak position in ion therapy by means of single photon detection. Radiat. Environ. Biophys. 2010;49:337-43.

[13] Smeets J, Roellinghoff F, Prieels D, Stichelbaut F, Benilov A, Busca P, et al. Prompt gamma imaging with slit camera for real-time range control in proton therapy. Phys. Med. Biol. 2012;57:3371-405.

[14] Bom V, Joulaeizadeh L, Beekman F. Real-time prompt gamma monitoring in spot-scanning proton therapy using imaging through a knife-edge-shaped slit. Phys. Med. Biol. 2012;57:297-308.

[15] Perali I, Celani A, Bombelli L, Fiorini C, Camera F, Clemental E, et al. Prompt gamma imaging of proton pencil beams at clinical dose rate. Phys. Med. Biol. 2014;59:5849-71.

[16] Min CH, Lee HR, Kim CH, Lee SB. Development of array-type prompt gamma measurement system for in vivo range verification in proton therapy. Med. Phys. 2012;39:2100-07.

[17] Peterson SW, Robertson D, Polf J. Optimizing a three-stage Compton camera for measuring prompt gamma rays emitted during proton radiotherapy. Phys. Med. Biol. 2010;55:6841-56.

[18] Richard MH, Chevallier M, Dauvergne D, Freud N, Henriquet P, Le Foulher F, et al. Design guidelines for a double scattering Compton camera for prompt-γ imaging during ion beam therapy: a Monte Carlo simulation study. IEEE Trans. Nucl. Sci. 2011;58:87-94.

[19] Biegun AK, Seravalli E, Lopes PC, Rinaldi I, Pinto M, Oxley DC, et al. Time-of-flight neutron rejection to improve prompt gamma imaging for proton range verification: a simulation study. Phys. Med. Biol. 2012;57:6429-44.

[20] Janssen FMFC, Landry G, Cambraia Lopes P, Dedes G, Smeets, J, Schaart DR, et al. Factors influencing the accuracy of beam range estimation in proton therapy using prompt gamma emission. Phys. Med. Biol. 2014;59:4427-41.

[21] Verburg JM, Riley K, Bortfeld T, Seco J. Energy and time resolved detection of prompt gamma rays for proton range verification. Phys. Med. Biol. 2013;58:L37-L49.

[22] Verburg JM, Seco J. Proton range verification through prompt gamma-ray spectroscopy. Phys. Med. Biol. 2014;59:7089-106.

[23] Agostinelli S, Allison J, Amako K, Apostolakis J, Araujo H, Arce P, et al. Geant4–a simulation toolkit. Nucl. Instrum. Methods Phys. Res. A. 2003;506:250-303.

[24] Allison J, Amako K, Apostolakis J, Araujo H, Arce P, Asai M, et al. Geant4 developments and applications. IEEE Trans. Nucl. Sci. 2006;53:270-8.

[25] Zacharatou JC, Paganetti H, Physics settings for using the Geant4 toolkit in proton therapy, IEEE Trans. Nucl. Sci. 2008;55:1018-25.